Geochemical Perspectives Letters

Earth's foundational geological events stored in the fundamental mantle source of hotspots

B.J. Peters, F. Nauret, B. Moine, P. Castillo

Supplementary Information

The Supplementary Information includes:

- Supplementary Materials and Methods Information
- Supplementary Information Regarding the Machine Learning Model
- Tables S-1 to S-6
- Figures S-1 to S-7
- Supplementary Information References

Supplementary Materials and Methods Information

Ocean island basalts (OIB) from two islands of the Crozet hotspot (Possession and Penguin) and two islands of the Juan Fernandez hotspot (Alexander Selkirk/Más Afuera and Robinson Crusoe/Más a Tierra) were selected for analysis. Major and trace element and He-Sr-^{143}Nd-Pb isotopic data were previously published for most samples (Farley, 1993; Breton *et al*., 2013; Truong *et al.*, 2018) and are supplemented in this study. Additionally, Os (Paquet *et al.*, 2019) and W (Mundl-Petermeier *et al.*, 2020) isotopic data are available for some of the studied OIB from Juan Fernandez (**Table S-1**). Juan Fernandez samples are primarily tholeiitic and represent the main stage of shield building on each island, with a minority of alkali basalts (MF-S1, PF-5, PV-2) and basanites (PF-16, PV-1). There is no systematic difference between the μ^{142}Nd compositions of tholeiitic and alkalic basalts (**Fig. 2**). Crozet samples with major element data are transitional tholeiitic to basanitic, however major element data are only available for 9 of the 17 studied samples.

The Sr-^{143}Nd-Pb isotopic compositions of all samples overlap with the broadly-defined compositional range of focus zone (FOZO) OIB (see comparison of interpreted FOZO compositional ranges in Stracke *et al.*, 2005) with each island defining a relatively homogeneous composition (**Fig. 3**). Possession Island OIB have slightly higher $^{87}Sr/^{87}Sr$ (average: 0.7042 ± 0.0003, 2 s.d.) than Penguin or Juan Fernandez OIB and thus lie on the outer edge of previously-defined FOZO ranges (*e.g.*, Hart *et al.*, 1992). These samples were previously interpreted to contain a minor enriched mantle (EM) component compared to Penguin Island samples (Breton *et al.*, 2013) and this perspective is evaluated in our mixing models (**Fig. 3**).

New Sr and Pb isotopic data were obtained for select Crozet samples to complement published data (Breton *et al.*, 2013) and are summarized in **Table S-1** and tabulated in full in **Tables S-4** and **S-5**. Lead was separated from sample matrix, including Sr, on BioRad® AG1-X8, 100-200 mesh anion exchange resin using mixed HBr-HNO_3 solutions. Strontium, Rb, and other minor elements were then separated from sample matrix on BioRad® AG50-X8, 200-400 mesh cation exchange resin using 2M HCl. Finally, Sr was purified using Eichrom® Sr resin using solutions with

variable HNO_3 concentrations. Strontium isotopic compositions were measured on the Triton TIMS in the Isotope Geochemistry and Cosmochemistry group at ETH Zürich using a static acquisition method with amplifier rotation. Data were normalized to an $^{88}Sr/^{86}Sr$ value of 8.375209 using the exponential law. Repeated measurements of the NBS987 standard in the same analytical session yielded an average $^{87}Sr/^{86}Sr$ value of 0.710270 ± 0.000011 (2 s.d.) and samples were re-normalized using a reference $^{87}Sr/^{86}Sr$ value for NBS987 of 0.710245 (mean of published values in the GeoREM database).

Lead isotopic compositions were measured on a Thermo Fisher NeptunePlus inductively coupled plasma mass spectrometer (ICP-MS) in the Isotope Geochemistry and Cosmochemistry group at ETH using a static acquisition method with amplifier rotation. Correction for instrumental mass bias was done using Tl doping and a $^{203}Tl/^{205}Tl$ ratio that was iteratively optimized in order to eliminate the summed offset between average measured $^{206,207,208}Pb/^{204}Pb$ and $^{207,208}Pb/^{206}Pb$ values of standard NBS981 and the reference values of (Baker *et al.*, 2004). The 2σ standard deviations of measured NBS981 across all analytical sessions were 0.007–0.0019 for $^{206}Pb/^{204}Pb$, 0.0007–0.0022 for $^{207}Pb/^{204}Pb$, and 0.0020–0.0059 for $^{208}Pb/^{204}Pb$. Repeated measurements (n = 15) of the BHVO-2 reference material (United States Geological Survey) produced an average $^{206}Pb/^{204}Pb$ of 18.6195 ± 0.0002 (95% c.i., GeoREM preferred: 18.634 ± 0.068), average $^{207}Pb/^{204}Pb$ of 15.5417 ± 0.0001 (95 % c.i., GeoREM preferred: 15.524 ± 0.050), and average $^{208}Pb/^{204}Pb$ of 38.2378 ± 0.0004 (95 % c.i., GeoREM preferred: 38.146 ± 0.646).

Neodymium isotopic compositions were determined on separate sample aliquots from those used for Sr-Pb isotopic measurements. Neodymium was separated from matrix material using three different methods: (1) a four-step method adapted from (Garçon *et al.*, 2018) (designated LN Chrom in **Table S-2**), (2) a two-step protocol utilizing BioRad AG50-X8 resin (Garçon *et al.*, 2018) and a tandem LN resin-DGA resin column adapted from (Chu *et al.*, 2019) and (Wang and Carlson, 2022) (designated cation-DGA in **Table S-2**), or (3) a three-step protocol with matrix separation on DGA resin (Chu, 2020), Ce separation using a tandem LN-DGA column (Wang and Carlson, 2022), and a final step to separate La, Ce, and Pr on a long-aspect (6 mm inner diameter x 6 cm length) Teflon column. Replicate measurements of the BHVO2 reference material using these three methods produced indistinguishable results (**Table S-2**), meaning that no method produced appreciable isotopic fractionation relative to another. Yields for method (1) were typically 70–90 % and yields for methods (2) and (3) were typically 80–100 %. Both methods produced similar Ce-Nd and Nd-Sm separation, but method (3) produced substantially better Pr-Nd separation than either method (1) or method (2).

Isotopic compositions of Nd were measured on the Thermo Fisher Triton thermal ionisation mass spectrometer in the Isotope Geochemistry and Cosmochemistry group at ETH using a 4-step multi-dynamic method adapted from (Garçon *et al.*, 2018). All Nd isotopic ratios were normalized to a $^{146}Nd/^{144}Nd$ ratio of 0.7219 using the exponential law and were corrected to account for the difference in time at which $^{146}Nd/^{144}Nd$ ratios were measured (*e.g.*, lines 1 and 2 for $^{142}Nd/^{144}Nd$) and the times at which the Nd isotope ratios of interest were measured (*e.g.*, lines 3 and 4 for $^{142}Nd/^{144}Nd$). Data were thoroughly checked for signs of non-exponential (Andreasen and Sharma, 2009) or anomalously fast (*e.g.*, Roth *et al.*, 2013) mass fractionation and runs were filtered or rejected when these effects could not be adequately constrained by the reduction (ca. 10 % of all runs). The medium-term precision of $\mu^{142}Nd$ is estimated as the drift-corrected 2 s.d. of all JNdi-1 standard runs from all instrument users between replacements of Faraday cup liners and was 5.2-6.9 ppm over three sets of cup liners. Uncertainty on single measurements was estimated to be the largest of (1) the medium-term uncertainty, (2) the 2 s.e.m. of the measurement (typically ca. 2 ppm), or (3) the 2σ standard deviation of all JNdi-1 standard runs in the same barrel as the sample (0.8–6.9 ppm, average 4.5 ppm). Uncertainty on replicate measurements of the same sample was calculated using Isoplot (Ludwig, 2003) as the weighted 95 % confidence interval (c.i.) of all replicate measurements with input uncertainties for individual measurements as defined above. Systematic effects on data accuracy were monitored through repeated dissolutions of the BHVO-2 reference material, which produced an average $\mu^{142}Nd$ of +0.7 ± 1.7 (n = 11) over the timeframe of this project, a value that is consistent with published ICPMS (*e.g.*, Saji *et al.*, 2016) and TIMS (*e.g.*,

Wang and Carlson, 2022) data. Further, these data show no correlation between different Nd isotopic ratios and no correlation between post-separation Nd yield and Nd isotopic ratios.

Supplementary Information Regarding the Machine Learning Model

Our clustering model utilized data accessed from the pre-compiled data files (December 2023 version) on GEOROC (DIGIS Team, Geoscience Centre Göttingen). No short-lived radiogenic data were used in the model, since the available number of samples with complete long-lived and short-lived isotopic data is too small to permit quantitative analysis with machine learning models. The data were first filtered to include only bulk rock analyses for rock names corresponding to intermediate-mafic volcanic rocks. In cases where the rock name was not given, rocks with SiO_2 contents between 40 and 65 wt. % were utilized. Following this, duplicate entries for the same sample (*e.g.*, multiple analyses of the same analyte) were aggregated and unweighted averages were taken for duplicated data. All forms of He ($^3He/^4He$, $^4He/^3He$, and these ratios normalized to those of air) and Nd ($^{143}Nd/^{144}Nd$ and $\varepsilon^{143}Nd$) isotopic data were reconciled. Sub-datasets were then created for samples that possessed Sr-^{143}Nd-Pb isotopic data (n = 4340), He-Sr-^{143}Nd-Pb isotopic data (n = 444), and Sr-^{143}Nd-Pb isotopic data plus abundances for Nb, Ba, La, Ce, Pb, and U (n = 2571). These trace element abundances were used to calculate Nb/U, Ce/Pb, and Ba/La ratios for use in the model, which are often considered to be relatively unchanged by partial melting and magma differentiation processes and are thus utilized to investigate OIB mantle sources (*e.g.*, Cordier *et al.*, 2021). Each sample in each sub-dataset must possess data for all analytes in a given sub-dataset in order to be used in the analysis. The data were then normalized on a linear scale of 0 to 1 with 0 representing the minimum value for a given analyte present in a sub-dataset and 1 representing the maximum.

Dimensionality reduction was accomplished using a t-distributed stochastic neighbour embedding (t-SNE) model to produce two-dimensional data from five- to eight-dimensional data in the original sub-datasets. A random state of 23 was employed for all models. Input perplexity was optimized using the Kullback-Leibler divergence over a perplexity range of 10-110 (**Fig. S-1**). The calculated divergence decreased with increasing perplexity over the entire tested range of perplexity, even well above the generally recommended maximum perplexity of 50. In general, higher perplexities caused the data to be divided into clusters that that were increasingly further apart from each other. At intermediate perplexities, more discrete clusters were visible, but with less separation between clusters. We were unable to reproduce cluster separation to the degree observed by (Stracke *et al.*, 2022), who reported that they used perplexity values between 25 and 45. There are many possible reasons for this discrepancy, since t-SNE is also sensitive to other inputs such as random state and data normalisation. For our models, we selected a perplexity of 70 as a compromise between the recommended maximum and the desire to minimise divergence as much as possible.

When applied to each sub-dataset, the t-SNE dimensionality reduction produced distinct results (**Fig. S-2**). The Sr-^{143}Nd-Pb isotopic sub-dataset produced the clearest visually-identified groups at a given input perplexity. By contrast, including trace element ratios Ce/Pb, Nb/U, and Ba/La decreased separation between groups. However, HIMU-type samples from the Austral-Cook hotspot formed a discrete group with greater separation compared to results from the Sr-^{143}Nd-Pb isotopic dataset. The sub-dataset including He isotopic compositions produced two broad groups, one of which was comprised of Hawaii and Iceland OIB while the other represented most other hotspots together. Samples from the Galápagos Islands formed a 'bridge' between these two broad groups (**Fig. S-2c**), with the intersection point between this bridge and the Hawaii-Iceland sample group consisting primarily of the highest $^3He/^4He$ samples from these three hotspots and Samoa. Due to the complexity in interpreting these results, we elected to proceed with only the Sr-^{143}Nd-Pb sub-dataset, however we provide comparative results for each sub-dataset in each figure for guidance. At an input perplexities ≥30, t-SNE reduction on this sub-dataset produced groups with broad relationships to recognized mantle geochemical components and endmembers (*e.g.*, **Fig. S-3**). Samples with the most depleted isotopic compositions plotted near the t-SNE variable origin, where some of the groups come together. Samples with progressively more enriched isotopic compositions plotted further away from the origin, with distinct radial pathways for samples with EM and HIMU affinity. Hawaii and Iceland OIB with EM affinity, however, did not plot along the

same radial pathway as other EM-type lavas. Instead, these two hotspots defined their own large group with the most EM-like samples plotting furthest away from the origin.

The t-SNE reduced data where then subjected to a K-means clustering model to provide a quantitative division between visually identified clusters, with no specified number of data points per cluster. K-means clustering models are significantly less computationally expensive than agglomerative clustering models (*e.g.*, Stracke *et al.*, 2022; White *et al.*, 2025) and rely on Euclidian distance between data points, which is independent of the size or composition of input datasets. However, they have the disadvantage that the number of clusters must be specified in advance, which decreases the objectivity of the model in evaluating the presence of discrete geochemical compositions. However, the selected number of clusters can be optimized for example using the silhouette score, which evaluates how similar each data point is to its assigned cluster compared to its similarity to other clusters. Low silhouette scores indicate that data points generally display high spatial affinity to their assigned clusters, whereas high scores reflect more ambiguous cluster assignments. We calculated the silhouette scores for models with 2 to 40 clusters (**Fig. S-4**). In general, we found that a local minimum in silhouette scores occurred around a number of clusters that roughly corresponded to the number of well-defined mantle geochemical components (n = 3–5: FOZO, DM, EM-1, EM-2, HIMU). The silhouette scores for all sub-datasets then increased after this point before reaching broad minimum plateaux at ≥15 clusters. This finding is similar to a recent study using agglomerative clustering (White *et al.*, 2025) but differs from a prior study that identified many more clusters using agglomerative clustering (Stracke *et al.*, 2022).

For visual inspection, cluster analysis was then performed using either 5 or 15 clusters (**Fig. S-5**). When the t-SNE reduced Sr-^{143}Nd-Pb isotopic sub-dataset is divided into five clusters (labelled 0–4), the K-means algorithm produces two large clusters for Hawaii and Iceland samples (clusters 0 and 3), with one cluster containing nearly exclusively Hawaii OIB and the second covering mainly the area of overlap between these two hotspots, plus one visually distinct sample group that contains Hawaii, Iceland, and Galápagos OIB. Cluster 2 contains most remaining Galápagos OIB, plus most Pitcairn and Penguin Island OIB as well as a radially protruding arm representing HIMU-type OIB from the Austral-Cook hotspot. Cluster 1 contains most Mascarene (Réunion), Samoa, and Possession Island samples and is the closest representative of a broad FOZO-like composition. Finally, cluster 4 is comprised primarily of Kerguelen and remaining Pitcairn OIB and thus roughly defines an EM-1 endmember cluster. Together, these assigned clusters reflect a relatively high-level view of global OIB compositions, with variable grouping of OIB traditionally assigned to different mantle geochemical components. However, there are some clear shortfalls to this relatively simplified clustering analysis. For example, HIMU-type OIB are clustered together with clearly non-HIMU OIB, and cluster 0 includes two TSNE sample groups with clear visual separation. Thus, it is most likely that five clusters underestimate the dispersion present in the data.

When instead fifteen clusters are assumed, many of these divisions are further granulated (**Fig. S-5**). The cluster consisting nearly entirely of Hawaii OIB is split into four distinct clusters, and the cluster representing Hawaii plus Iceland and Galápagos OIB is likewise split into four separate clusters. One of these clusters represents the visually distinct group of samples that comprises overlapping t-SNE variable values for Hawaii, Iceland, and Galápagos data together. The HIMU-type OIB are split into a separate cluster, but the former EM-1 cluster is likewise split into two clusters that do not correspond to the two primary hotspots comprising this group. Similarly, the cluster corresponding most closely to FOZO-type hotspots was split into two clusters, with some Juan Fernandez samples present in each cluster. It is therefore evaluated that assigning fifteen clusters to the data overestimates the spatial distinction between global OIB data. However, this granularity is useful to identify and filter out clusters not clearly associated with FOZO-like compositions.

Using this baseline clustering analysis, we removed clusters representing OIB with isotopic compositions clearly more depleted or enriched than a broadly defined FOZO range. Of the fifteen originally defined clusters, eight were removed on the basis of isotopic affinity to non-FOZO mantle endmembers like EM and HIMU (*e.g.*, Stracke *et al.*,

2005). This selection enabled filtering on a per-sample basis, which avoids excluding entire hotspots because some lavas from that hotspot have isotopic affinity to a non-FOZO endmember. However, this meant that two samples from the Juan Fernandez hotspot with slightly more enriched isotopic compositions (Gerlach *et al.*, 1986) than those measured in this study were selectively removed because they were quantitatively clustered with other samples possessing isotopic compositions trending toward an EM1-like endmember. All samples measured for their μ^{142}Nd compositions in this study were retained by this filtering, presenting a semi-objective confirmation that they are close representatives of global FOZO compositions. Following this, t-SNE dimensionality reduction was repeated on the filtered database. Perplexity was again optimized but the result was similar to the full dataset and a perplexity value of 70 was thus maintained. The number of quantitatively identified clusters was again optimized, which revealed an absence of the local minima of silhouette scores previously identified and broad plateaux of silhouette scores with $n_{clusters} \geq 15$ and especially for $n_{clusters} \geq 35$.

The t-SNE reduction of FOZO hotspots revealed three visually distinct groups (**Fig. S-6**). One group again corresponds to nearly all Hawaii and most Iceland samples. The persistence of this unique group in all TSNE analyses (*e.g.*, **Figs. 4**, **S-2**) is remarkable and implies that the commonality of the FOZO component of these hotspots should be investigated in more detail. The second group is comprised primarily of Galápagos and Pitcairn samples, along with remaining Iceland samples, all but one of the Penguin Island samples, and FOZO-type samples from the Cook-Austral hotspot. The third group consists of Juan Fernandez samples, the remaining Penguin Island sample, all Possession Island samples, Mascarene OIB, and FOZO-type Samoa OIB. Quantitative clustering analysis assuming 15 clusters splits each of these groups into 4–6 clusters without clear relationship to sample origin. Nevertheless, the use of at least 15 clusters is justified by decreasing silhouette scores with increasing cluster counts, implying that the spatial separation of these clusters in five dimensions (i.e. the number of isotope analytes) is quantitatively justified. However, regardless of whether one considers the visual separation (3 groups) or the quantitative separation (≥15 clusters), it is clear that FOZO-type OIB have multi-nodal long-lived radiogenic isotopic compositions. The short-lived radiogenic isotopic compositions of these samples implies that their distinctness is still greater than what is implied by this analysis. For example, the He-W isotopic compositions of Hawaii and Samoa OIB plot on the same trend (Mundl-Petermeier *et al.*, 2020), but their Sr-^{143}Nd-Pb isotopic compositions are visually and quantitatively distinct after t-SNE reduction. Further, Crozet samples display statistically indistinct μ^{142}Nd compositions (**Fig. 2**) but plot in visually and quantitatively distinct groups or clusters. However, the apparently greater internal μ^{142}Nd heterogeneity among Penguin Island OIB may imply that this similarity represents the analytical limitations still associated with μ^{142}Nd analysis. Future incorporation of short-lived radiogenic isotopic compositions into machine learning models like this one may reveal that the division of FOZO-like OIB into many clusters, as implied by our analysis, is further justified and that FOZO-type OIB represent many diverse geological histories stored in Earth's mantle.

The diverse isotopic compositions of FOZO-like OIB are not easy to reconcile with the two well-defined large low shear wave velocity provinces (LLSVP) in Earth's deep mantle. This is even clearer when considering the clear geochemical association of FOZO-type OIB, such as those from the Hawaii and Iceland hotspots, that are spatially near different LLSVP. Independent analysis of hotspots surrounding LLSVP have revealed a closer spatial association of LLSVP with isotopic compositions indicative of long-term tectonic recycling (Jackson *et al.*, 2018), rather than FOZO-like compositions. If the quantitative clustering model we employ is correct in predicting the existence of many FOZO-like compositional domains, it may be difficult to store these compositions in singular domains over geological timescales without mixing them together. The implication of our machine learning model is instead that FOZO-like domains are discrete, numerous, and small enough to only be sampled over short spatial scales by a limited number of hotspots.

Supplementary Tables

Tables S-1 to S-6 are available for download (.xlsx) from the online version of this article at https://doi.org/10.7185/geochemlet.2553.

Table S-1 Per-sample isotopic data.

Table S-2 Per-run TIMS Nd isotopic data.

Table S-3 Medium-term precision of Nd isotopic ratios.

Table S-4 TIMS Sr isotopic data.

Table S-5 ICP-MS Pb isotopic data.

Table S-6 Inputs to binary mixing models in Figure 2.

Supplementary Figures

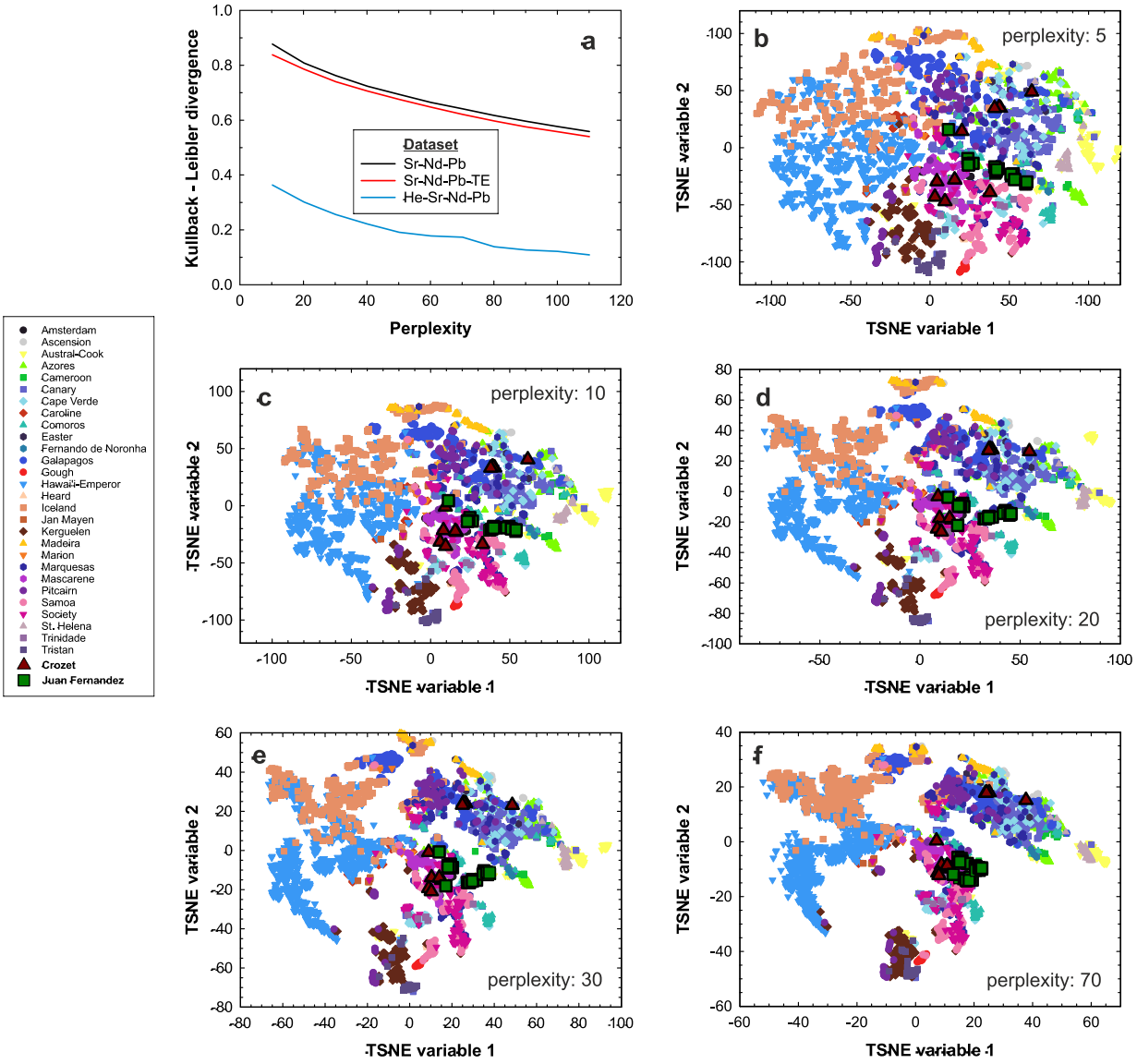

Figure S-1 Optimisation of perplexity in t-SNE dimensionality reduction and examples of t-SNE reduced data with variable perplexity.

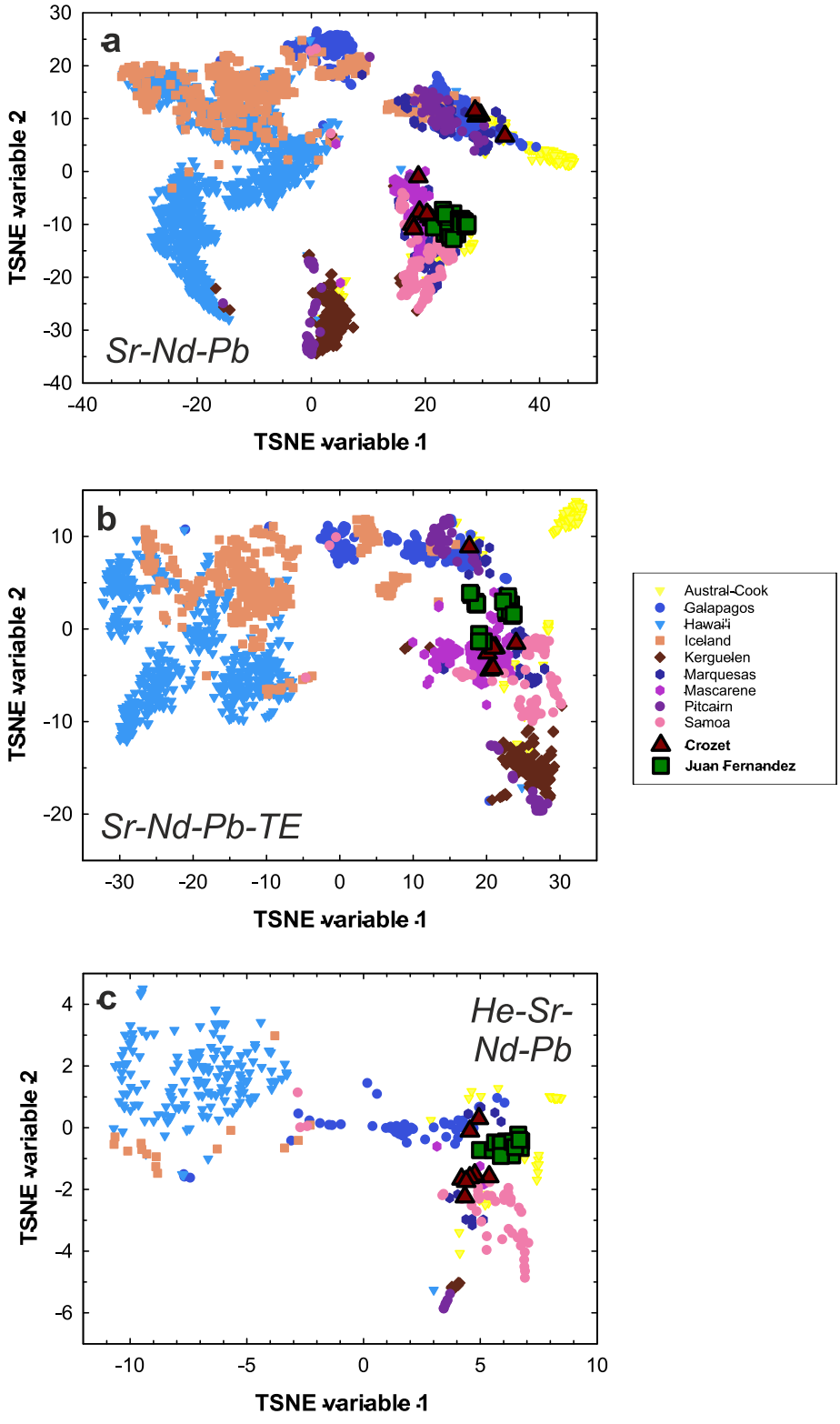

Figure S-2 Comparison of t-SNE reduction for sub-datasets including only Sr-^{143}Nd-Pb isotopic compositions **(a)** and those additionally including **(b)** trace element (Nb/U, Ce/Pb, and Ba/La ratios) or **(c)** He isotopic compositions. For all models, perplexity is set at 70.

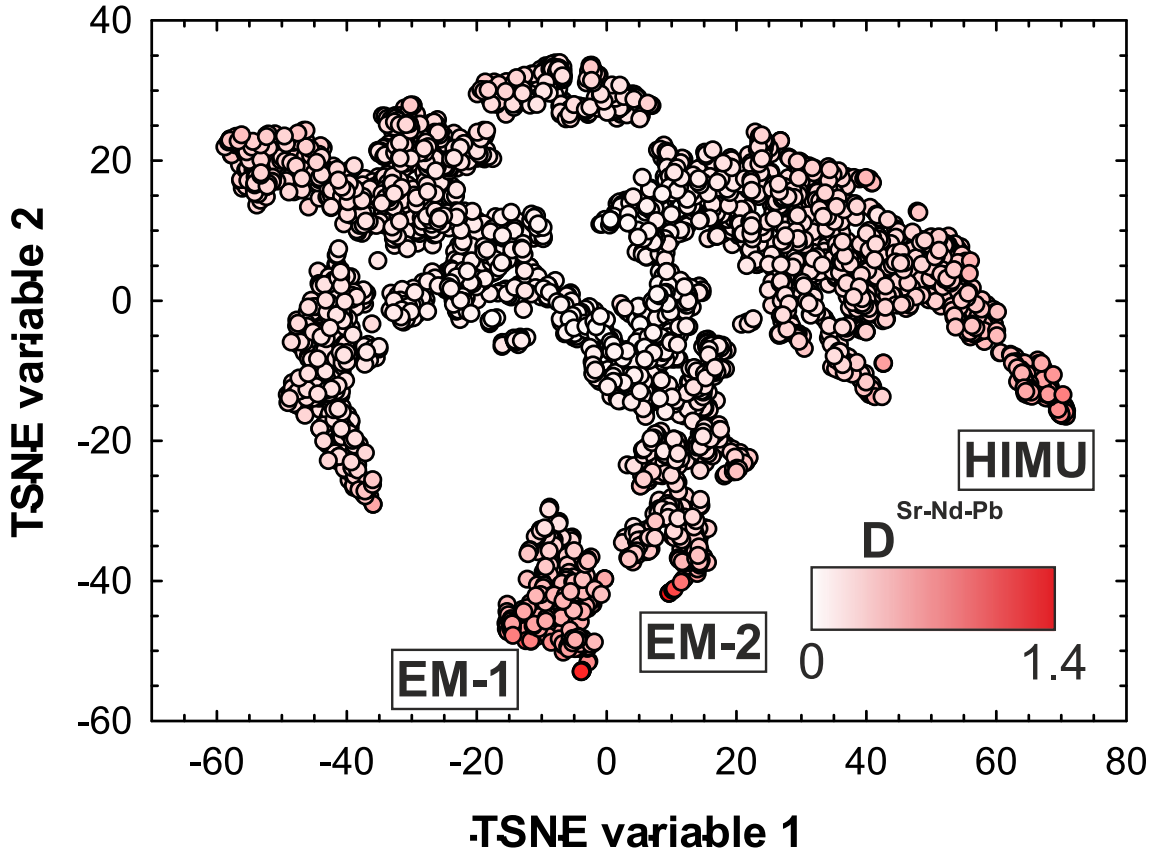

Figure S-3 Reduced-dimension OIB data for selected hotspots (as in **Fig. S-2**) with a perplexity of 30 to emphasise visual grouping (*cf.*, **Fig. S-2e**). Individual data points are colour coded for their $D^{Sr\text{-}Nd\text{-}Pb}$ values, which index their Sr-^{143}Nd-^{206}Pb isotopic compositions against a reference depleted composition (≡0) (after Jackson *et al.*, 2020). The most isotopically depleted samples plot near the origin (t-SNE variable 1 = 0, t-SNE variable 2 = 0) and $D^{Sr\text{-}Nd\text{-}Pb}$ values increase radially, with the closest associations to EM- and HIMU-type OIB on the outside of the diagram. However, the spatial distance between samples with moderate $D^{Sr\text{-}Nd\text{-}Pb}$ values at different radial locations implies that they have differing multi-dimensional isotopic compositions even when their isotopic compositions appear to overlap on binary isotope plots (*e.g.*, **Fig. 1a**).

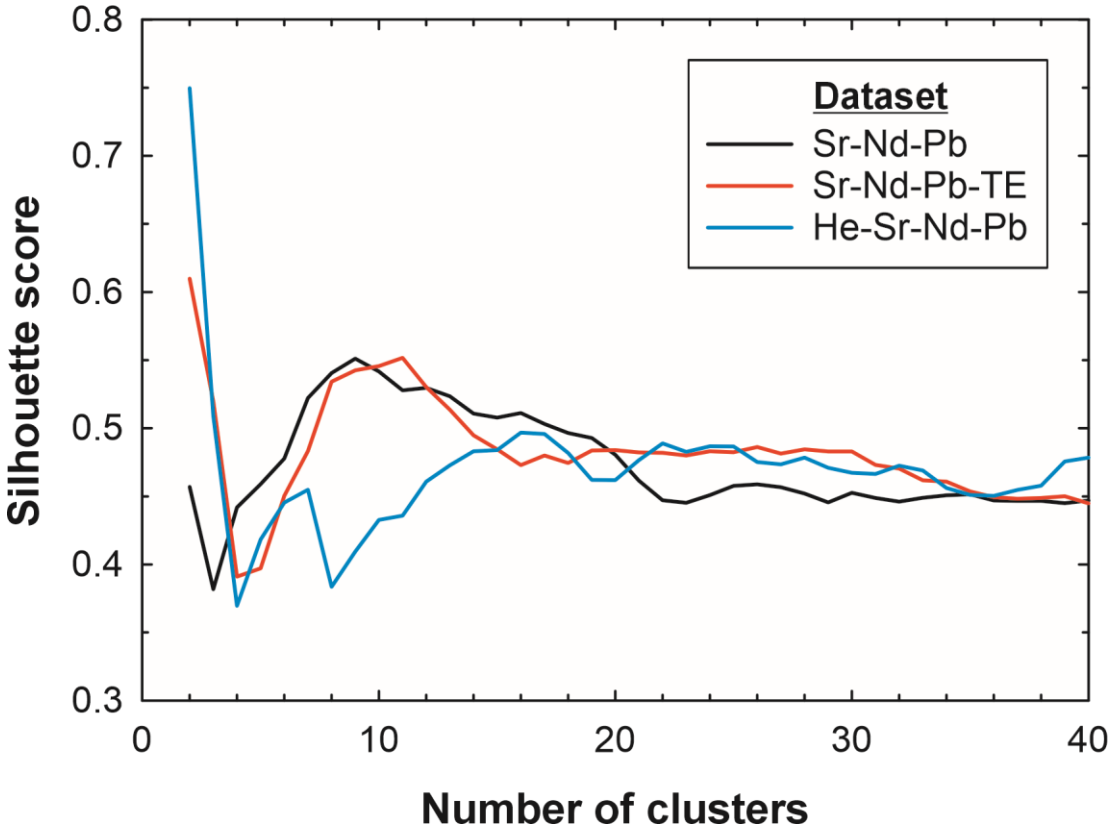

Figure S-4 Optimisation of input cluster counts for K-means cluster analysis. Silhouette score (y-axis) measures the average affinity of each data point for its assigned cluster with higher values indicating less affinity.

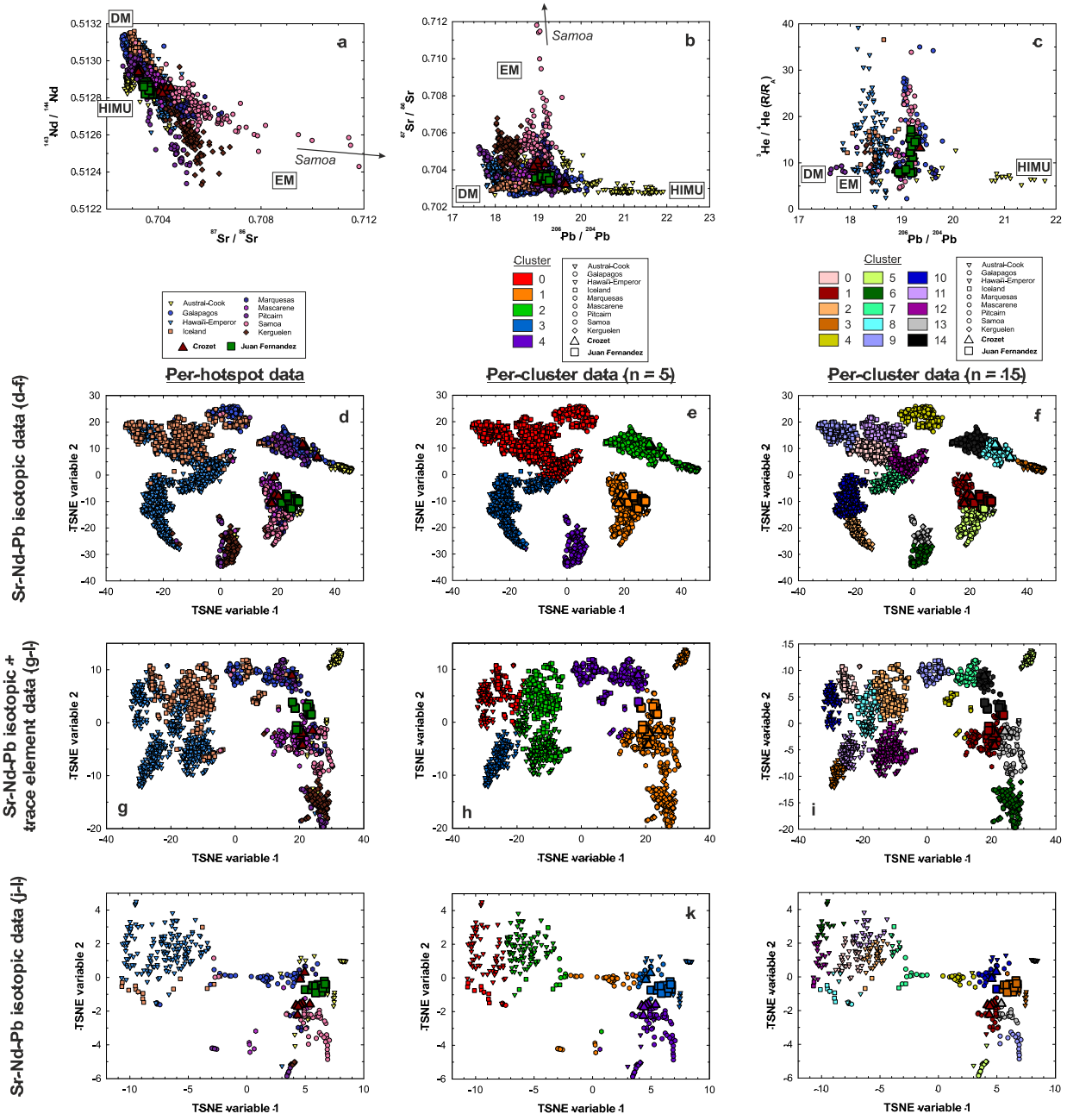

Figure S-5 Comparison of clustering behavior in 9 key hotspots for different sub-datasets (rows, except for first row) and different defined numbers of clusters (columns, except for first column). Data in the first row and first column are colour coded according to their hotspot whereas data in the remaining panels are colour coded according to their assigned cluster. Reducing the data analysis to 9 key hotspots significantly decreased the computational expense of the model and also simplifies visualisation (*cf.*, **Figure S-1**).

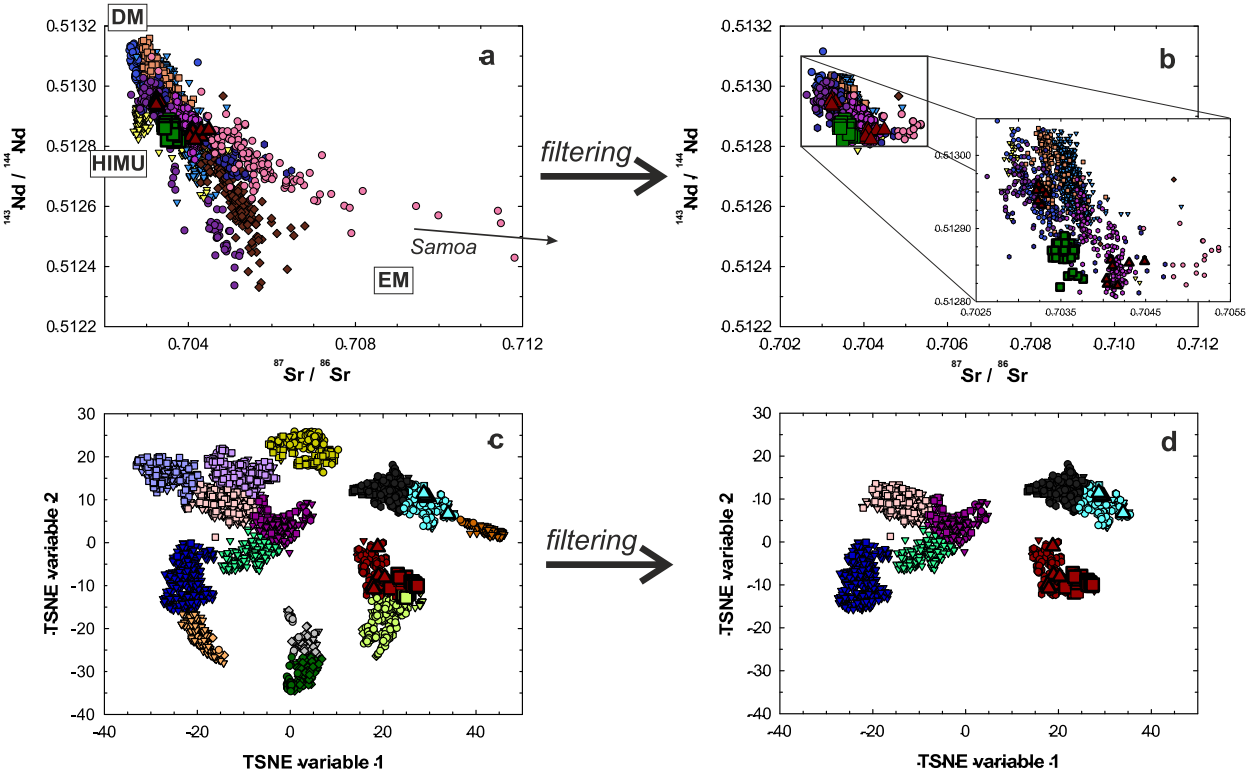

Figure S-6 Filtering of data according to assigned cluster (n = 15) to keep only data from clusters that strongly overlap with a broad FOZO-like isotopic range. In panels **(a)** and **(b)** data are colour coded by hotspot, and in panels **(c)** and **(d)** they are colour coded by cluster (*cf.*, **Fig. S-5**).

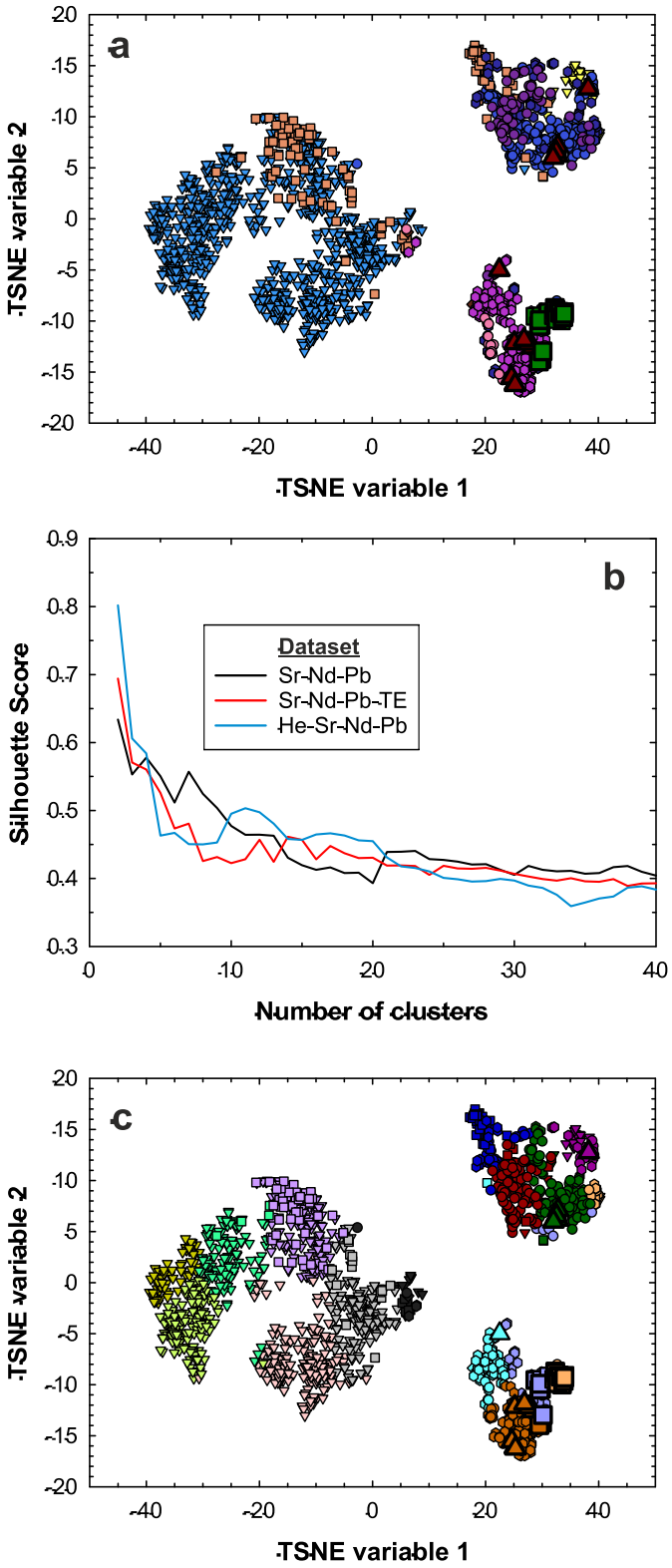

Figure S-7 Result of re-calculated t-SNE and K-means models for data filtered for FOZO affinity. In panel **(a)**, symbol colouring corresponds to that in **Fig. S-5**. In panel **(b)**, the same colours are used for each cluster as in **Fig. S-5**, but note that due to the recalculation after filtering these now represent different clusters.

Supplementary Information References

Andreasen, R., Sharma, M. (2009) Fractionation and mixing in a thermal ionization mass spectrometer source: Implications and limitations for high-precision Nd isotope analyses. *International Journal of Mass Spectrometry* 285, 49-57. https://doi.org/10.1016/j.ijms.2009.04.004

Baker, J., Peate, D., Waight, T., Meyzen, C. (2004) Pb isotopic analysis of standards and samples using a 207Pb–204Pb double spike and thallium to correct for mass bias with a double-focusing MC-ICP-MS. *Chemical Geology* 211, 275-303. https://doi.org/10.1016/j.chemgeo.2004.06.030

Breton, T., Nauret, F., Pichat, S., Moine, B., Moreira, M., Rose-Koga, E.F., Auclair, D., Bosq, C., Wavrant, L.-M. (2013) Geochemical heterogeneities within the Crozet hotspot. *Earth and Planetary Science Letters 376*, 126-136. https://doi.org/10.1016/j.epsl.2013.06.020

Chu, Z.-Y., Wang, M.-J., Li, C.-F., Yang, Y.-H., Xu, J.-J., Wang, W., Guo, J.-H. (2019) Separation of Nd from geological samples by a single TODGA resin column for high precision Nd isotope analysis as NdO+ by TIMS. *Journal of Analytical Atomic Spectrometry* 34, 2053-2060. https://doi.org/10.1039/C9JA00200F

Chu, Z. (2020) Analytical Methods for Os Isotope Ratios and Re-PGE Mass Fractions in Geological Samples. *Frontiers in Chemistry* 8, 615839. https://doi.org/10.3389/fchem.2020.615839

Cordier, C., Delavault, H., Chauvel, C. (2021) Geochemistry of the Society and Pitcairn-Gambier mantle plumes: What they share and do not share. *Geochimica et Cosmochimica Acta* 306, 362-384. https://doi.org/10.1016/j.gca.2021.04.014

Farley, K.A.B., Basu, A.R., Craig, H. (1993) He, Sr and Nd isotopic variations in lavas from the Juan Fernandez Archipelago, SE Pacific. *Contributions to Mineralogy and Petrology* 115, 75-87. https://doi.org/10.1007/BF00712980

Garçon, M., Boyet, M., Carlson, R.W., Horan, M.F., Auclair, D., Mock, T.D. (2018) Factors influencing the precision and accuracy of Nd isotope measurements by thermal ionization mass spectrometry. *Chemical Geology* 476, 493-514. https://doi.org/10.1016/j.chemgeo.2017.12.003

Gerlach, D.C., Hart, S.R., Morales, V.W.J., Palacios, C. (1986) Mantle heterogeneity beneath the Nazca plate: San Felix and Juan Fernandez islands. *Nature* 322, 165-169. https://doi.org/10.1038/322165a0

Hart, S.R., Hauri, E.H., Oschmann, L.A., Whitehead, J.A. (1992) Mantle Plumes and Entrainment: Isotopic Evidence. *Science* 256, 517-520. https://doi.org/10.1126/science.256.5056.517

Jackson, M.G., Becker, T.W., Konter, J.G. (2018) Geochemistry and Distribution of Recycled Domains in the Mantle Inferred From Nd and Pb Isotopes in Oceanic Hot Spots: Implications for Storage in the Large Low Shear Wave Velocity Provinces. *Geochemistry, Geophysics, Geosystems* 19, 3496-3519. https://doi.org/10.1029/2018GC007552

Jackson, M.G., Blichert-Toft, J., Halldorsson, S.A., Mundl-Petermeier, A., Bizimis, M., Kurz, M.D., Price, A.A., Harethardottir, S., Willhite, L.N., Breddam, K., Becker, T.W., Fischer, R.A. (2020) Ancient helium and tungsten isotopic signatures preserved in mantle domains least modified by crustal recycling. *Proceedings National Academy of Sciences USA* 117, 30993-31001. https://doi.org/10.1073/pnas.2009663117

Ludwig, K.R. (2003) Isoplot 3.00: A geochronological toolkit for Microsoft Excel. Berkeley Geochronology Center.

Mundl-Petermeier, A., Walker, R.J., Fischer, R.A., Lekic, V., Jackson, M.G., Kurz, M.D. (2020) Anomalous ^{182}W in high ^{3}He/^{4}He ocean island basalts: Fingerprints of Earth's core? *Geochimica et Cosmochimica Acta* 271, 194-211. https://doi.org/10.1016/j.gca.2019.12.020

Paquet, M., Day, J.M.D., Castillo, P.R. (2019) Osmium isotope evidence for a heterogeneous $^{3}He/^{4}He$ mantle plume beneath the Juan Fernandez Islands. *Geochimica et Cosmochimica Acta* 261, 1-19. https://doi.org/10.1016/j.gca.2019.06.039

Roth, A.S.G., Bourdon, B., Mojzsis, S.J., Touboul, M., Sprung, P., Guitreau, M., Blichert-Toft, J. (2013) Inherited ^{142}Nd anomalies in Eoarchean protoliths. *Earth and Planetary Science Letters* 361, 50-57. https://doi.org/10.1016/j.epsl.2012.11.023

Saji, N.S., Wielandt, D., Paton, C., Bizzarro, M. (2016) Ultra-high-precision Nd-isotope measurements of geological materials by MC-ICPMS. *Journal of Analytical Atomic Spectrometry* 31, 1490-1504. https://doi.org/10.1039/C6JA00064A

Stracke, A., Hofmann, A.W., Hart, S.R. (2005) FOZO, HIMU, and the rest of the mantle zoo. *Geochemistry, Geophysics, Geosystems* 6, Q05007. https://doi.org/10.1029/2004GC000824

Stracke, A., Willig, M., Genske, F., Béguelin, P., Todd, E. (2022) Chemical Geodynamics Insights From a Machine Learning Approach. *Geochemistry, Geophysics, Geosystems* 23, e2002GC010606. https://doi.org/10.1029/2022GC010606

Truong, T.B., Castillo, P.R., Hilton, D.R., Day, J.M.D. (2018) The trace element and Sr-Nd-Pb isotope geochemistry of Juan Fernandez lavas reveal variable contributions from a high-3He/4He mantle plume. *Chemical Geology* 476, 280-291. https://doi.org/10.1016/j.chemgeo.2017.11.024

Wang, D., Carlson, R.W. (2022) Tandem-column extraction chromatography for Nd separation: minimizing mass-independent isotope fractionation for ultrahigh-precision Nd isotope-ratio analysis. *Journal of Analytical Atomic Spectrometry* 37, 185-193. https://doi.org/10.1039/D1JA00365H

White, W.M., Jackson, M.G., Hardardottir, S. (2025) Insights Into Mantle Plume Geochemistry From Machine Learning. *Geochemistry, Geophysics, Geosystems* 26, e2024GC011870. https://doi.org/10.1029/2024GC011870